Journal of Innovative Optical Health Sciences
Vol. 2, No. 2 (2009) 165–177

World Scientific
www.worldscientific.com

A SIMULATION STUDY ON DYNAMIC-SAMPLING-MODE FOR FLUORESCENCE MOLECULAR TOMOGRAPHY

ZHUN XU* and JING BAI†
Department of Biomedical Engineering
School of Medicine, Tsinghua University
Beijing 100084, China
**zhun310@yahoo.com.cn*
†*deabj@tsinghua.edu.cn*

Fluorescence tomography can obtain a sufficient dataset and optimal three-dimensional images when projections are captured over 360° by CCD camera. Herein a non-stop dynamic sampling mode for fluorescence tomography is proposed in an attempt to improve the optical measurement speed of the traditional imaging system and stability of the object to be imaged. A series of simulations are carried out to evaluate the accuracy of dataset acquired from the dynamic sampling mode. Reconstruction with the corresponding data obtained in the dynamic-mode process is also performed with the phantom. The results demonstrate the feasibility of such an imaging mode when the angular velocity is set to the appropriate value, thus laying the foundation for real experiments to verify the superiority in performance of this new imaging mode over the traditional one.

Keywords: Fluorescence molecular tomography; dynamic sampling mode; simulation.

1. Introduction

Emerging as an important alternative for molecular imaging, fluorescence molecular tomography (FMT) is applied to probing the distribution of fluorescence reporters associated with cellular functions.[1–3] During the last decade, imaging systems for FMT have evolved over several generations from the early fiber-based systems[4,5] to the non-contact detection system of slab geometry based on CCD camera.[6] Moreover, the latter makes it possible to achieve high spatial sampling and leads to a sub-millimeter resolution. However, both systems require matching fluid, which is inconvenient for experiments. To get rid of the matching fluid[7] and enable experimental simplicity, implementation of free-space fluorescence tomography in the 360° geometry with CCD-camera-based detection was proposed in 2007, making it possible to yield a superior information content dataset.[2,8–10]

In such traditional free-space CCD-camera-based FMT, the rotation of phantom and the exposure of CCD camera are carried out alternately. When the motor stopped, the CCD camera began to capture the photons from the surface of phantom. It usually takes several seconds to collect sufficient fluorescent photons at each source projection position, and the acquisition time is relatively longer because the time spent on the rotation is wasted. Besides, due to the inertia effect, the soft tissue of an animal might be opposite to or move along with the rotational direction during the repetitive starting and stopping of the motor, which might cause

†Corresponding author.

the instability of the subject. In order to improve the optical measurement speed and reduce the unwanted soft tissue movements during living animal experiments when the scan rotation starts and stops, an imaging method of dynamic sampling, in which the object rotates continuously during imaging, is proposed. Such a dynamic sampling mode allows the synchronization of image capture and mechanical rotation. However, since the theory of reducing unwanted soft-tissue movements could be more appropriately validated through experiments, the main purpose of the work presented in this paper is only to investigate the feasibility of such an imaging mode through simulations, so as to lay the foundation for real experiments to verify the superiority in the stability and manipulation of this new imaging mode over the traditional one. The accuracy of the data collected in the dynamic mode is evaluated in the computer simulation experiments. How the inaccuracy of dynamic data might influence the reconstruction performance is also studied.

The paper is presented as follows. In Sec. 2, the method of calculating the object's surface data acquired by CCD camera in a dynamic sampling mode is described. Section 3 details the numerical experiments for evaluating the accuracy of the data from the dynamic mode. Reconstructions with dynamic sampling data are also performed in this section as a supplement to the study. Finally, the study results are discussed and concluded in Sec. 4.

2. Methodology

2.1. *Forward problem*

In a continuous wave (CW) fluorescence imaging experiment, the model of photon propagation can be described by the diffusion theory.[11–15]

The coupled diffusion equations are given by

$$\nabla \cdot [D_x(r)\nabla\Phi_x(r)] - \mu_{ax}(r)\Phi_x(r) = -\Theta_s\delta(r - r_{sl}), \quad (1)$$

$$\nabla \cdot [D_m(r)\nabla\Phi_m(r)] - \mu_{am}(r)\Phi_m(r) = -\Phi_x(r)\eta(r)\mu_{af}(r), \quad (2)$$

where r is the position vector, $\Phi_x(r)$ and $\Phi_m(r)$ represent the excitation and emission photon intensity (photons/cm^2/s) at position r respectively, $\mu_{ax,m}$ is the total absorption coefficient at the respective wavelengths, and $D_{x,m}$ is the optical diffusion coefficient equivalent to $1/3(\mu_{ax,m} + \mu'_{sx,m})$, where $\mu'_{sx,m}$ is the reduced scattering coefficient (cm^{-1}). $\eta(r)$ is the fluorophore's quantum efficiency and μ_{af} is the absorption coefficient due to fluorophores (cm^{-1}), which is directly proportional to the fluorophore concentration. r_{sl} $(l = 1, 2, \ldots, L)$ represents the different excitation point source positions with respect to the subject with the amplitude Θ_s. The coupled diffusion equations are supplemented by the Robin-type boundary conditions on the boundary.[17,18]

The finite element method (FEM) has been widely used to solve the partial differential equations (1) and (2). Two stiffness matrices are combined for each element, K_x for the excitation Eq. (1) and K_m for the emission Eq. (2). Then the solutions of Eqs. (1) and (2) are obtained by solving the matrix equation:

$$K_x\Phi_x = L_x, \quad (3)$$

$$K_m\Phi_m = Fx, \quad (4)$$

where L_x and Fx are the right-hand side of excitation and emission equations after the finite element transformation.[16]

For each r_{sl} $(l = 1, 2, \ldots, L)$, the corresponding $\Phi_{x,sl}$ is directly obtained by solving Eq. (3) since the stiff matrix K_x is symmetrical and positive definite. Then Eq. (4) can be changed to $\Phi_{m,sl} = K^{-1}_{m,sl} \cdot F \cdot x = Ax$ for each $\Phi_{x,sl}$.[19] Since $\Phi_{x,sl}$ includes the measurement on the boundary of phantom and the interior vertices, the rows of matrix A corresponding to the surface measurement can be chosen to form the new matrix equation $A_0x = m$, where m corresponds to the surface measurement. Based on the transformation that maps the surface points onto the CCD detector plane,[21,22] the matrix equation can be further written as $Wx = b$ where b is the measurement on the CCD plane.

2.2. *Simulation model*

In our FMT system, the object to be imaged rotates continuously at an appropriate speed during the experimental period. And the CCD camera is fixed on the opposite side of excitation light source to capture different views of the phantom surface while the phantom is rotating in the experiment. Thus, the rotating mode of the object is equivalent to the synchronous rotating modes of both CCD camera and laser system in the simulation process. Then the photon intensity of corresponding positions that the CCD camera would cover can be calculated.

$M(t)$ is defined as the image matrix at the time of t. Each element of the matrix represents the photon intensity acquired by the corresponding

position of CCD detector plane. Since a transformation can be determined that describes the contribution of the surface points onto a certain detector, the elements of $M(t)$ are calculated through the established relationship between the surface data and the values obtained by CCD camera.[21,22] Then the image processed during the continuous rotation process within a given exposure time T of CCD corresponds to that processed within the angular range of vT, where v is the angular velocity of the phantom. The image matrix can be described as:

$$M_T = \int_0^T M(t)dt. \tag{5}$$

In order to simulate the dynamic sampling process on computer, the time integral is transformed into the sum of image matrices obtained at different times, leading to

$$M_T^d = \sum_{i=0}^{n} M(i\Delta t)\Delta t. \tag{6}$$

Assuming T is normally discretized into n intervals, then $\Delta t = T/n$.

In our computer simulation, the image matrices acquired in both the dynamic sampling mode and the step-mode are compared. In the latter, a static image matrix obtained at the middle position of the rotation process of the dynamic sampling mode is selected as a reference matrix; for example, suppose the object rotates from 0° to 12° in dynamic sampling mode, the static image is acquired at an angle of 6°. Since the angular velocity is assumed constant, thus,

$$M_T^s = M(T/2)T. \tag{7}$$

Based on the quantitative analysis of the difference between M_T^d and M_T^s, the feasibility of dynamic mode to offer the accurate dataset is demonstrated.

2.3. *Reconstruction method*

To solve the matrix equation $Wx = b$ derived from diffusion equations with FEM,[17,18,21] Tikhonov regularization[20] is adopted. The regulation method is to make sure that the fluctuation of x is not that large when b contains measurement errors. That is,

$$Wx = \tilde{b}, \tag{8}$$

where $\|\tilde{b} - b\| \leq \delta$. The solution of Eq. (8) is the one that minimizes the following weighted combination of the residual norm and the side constraint:

$$\min_{x_{\inf} \leq x_k \leq x_{\sup}} \{\|Wx_k - b^{\text{mea}}\| + \alpha_k \eta_k(x_k)\}, \tag{9}$$

where $x_{\inf}$ and $x_{\sup}$ are the lower and upper bounds of $\eta\mu_{af}$, respectively. α_k is the regularization parameter and $\eta_k(x_k)$ is the penalty function. The iterative regularization method is used for image reconstruction.[19]

2.4. *Software implementation*

Our simulations are implemented with the software COMSOL Multiphysics 3.3, which has greatly facilitated the design and solution of PDE-based physical problems in FEM. Due to the ability to interface with MATLAB of COMSOL Multiphysics, the algorithm we have proposed is coded in MATLAB 7.1 for flexibility. The whole process of simulation is carried out on a Pentium 4, 1.5-GHz and 1-GB RAM computer.

3. Simulations and Results

A series of emulational experiments were designed to evaluate the accuracy of dynamic sampling process. A heterogeneous cylindrical phantom of 3-cm height and 1.5-cm radius was set up, which consisted of four ellipsoids and one cylinder to represent muscle, lungs, heart, bone and liver, as shown in Fig. 1. The phantom selected was the same as that used by Lv *et al.*[23] in their study on the bioluminescence tomography. Optical parameters from the literature[24] were assigned to those five organs, as listed in Table 1. They can be considered diffuse before detection according to the diffusion coefficient from Ref. 23.

In Table 1, D represents the diffusion coefficient with the expression that $D = 1/(3(\mu_a + (1-g)\mu_s(x)))$.

Fluorescent target, a sphere of 0.5 mm in diameter, was embedded in one of the lungs of the phantom (Fig. 2). The spots of 5×15 on the CCD plane (Fig. 2) were selected to form the image matrix. The excitation light source was on the surface of phantom at a height of 1.5 cm. In our simulations, the exposure time of CCD was set to 12 s, which was the same as that in our experiment. Eight projection positions were selected for the comparison of forward data and for the reconstruction in the simulations.

3.1. *Comparison between dynamic mode and step-mode with single target*

In this simulation, the accuracy of the image data and the reconstruction performance at two different

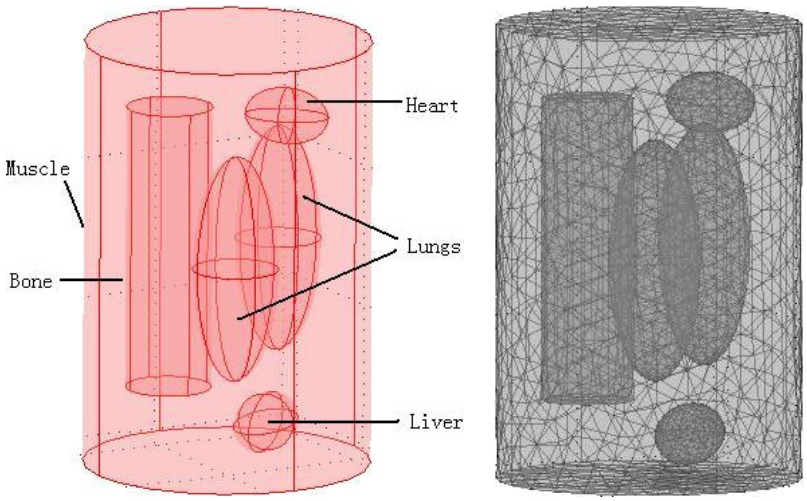

Fig. 1. Heterogeneous phantom. (a) The heterogeneous phantom on which the investments of dynamic sampling mode are performed. (b) The initial mesh obtained by COMSOL and used in the reconstruction.

Table 1. Optical parameters of the heterogeneous phantom.

Material	Muscle	Lung	Heart	Bone	Liver
$\mu_a[\text{mm}^{-1}]$	0.01	0.35	0.2	0.002	0.3
$D[\text{mm}]$	0.81	0.19	0.13	0.17	0.37

angular velocities in dynamic mode (1°/s and 2°/s), compared with step-mode, was investigated. In the rotation process, the speed of light was sufficiently high that the speed of rotation did not prevent photons from reaching the CCD, but it might prevent sufficiently long exposure time for weak fluorescent signals to be adequately detected. To simulate the rotation process, it was assumed that the number of $M(t)$ within the given angular range was constant. In the simulation of dynamic mode with angular velocity of 1°/s and exposure time of 12 s, Eqs. (6) and (7) can be expressed as

$$M_\theta^d = \sum_{i=0}^{24} M_\theta(i\Delta t)\Delta t, \quad \text{and}$$

$$M_\theta^s = 12M_\theta(6).$$

If the initial position is defined as 0° position, then $M_\theta(i\Delta t)$ represents the image obtained at the $(\theta + i\Delta t)$ position and M_θ^d represents the image obtained in the process of the phantom rotation from θ to $(\theta + 12°)$. Here we set $\Delta t = 0.5$ s in the simulation. It is known that the faster the phantom rotates, the less exposure time each photon will effectively have on the CCD. Assuming that it takes the same time for the photons at different projection positions effectively having on the CCD plane, when the angular velocity is 2°/s, Eqs. (6) and (7)

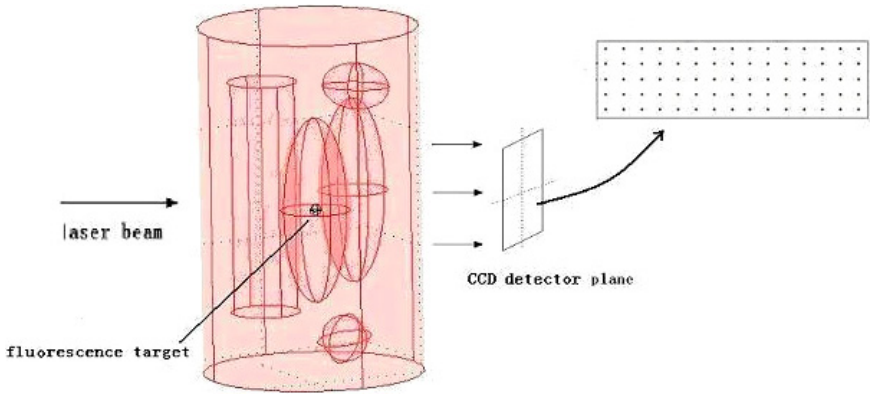

Fig. 2. The spots of 5×15 on the phantom surface in the camera field of view to form the image matrix.

can be expressed as

$$M_\theta^d = \sum_{i=0}^{48} M_\theta(i\Delta t)\frac{\Delta t}{2}, \quad \text{and}$$

$$M_\theta^s = 12M_\theta(12).$$

From Fig. 2, it can be seen that M_θ^d is a matrix of 5×15.

The average error at each projection position is defined as the expression below:

$$e_i = \left(\sum_{j=1}^{m} |d_{ij} - s_{ij}|/s_{ij}\right) \Big/ m, \qquad (10)$$

where d_{ij} is the accumulation result, mentioned in Sec. 2.2, to simulate the reading that forms the jth camera pixel after ith exposure (the ith projection position), and s_{ij} is the reading that forms the jth camera pixel after ith exposure in step-mode. m represents the discrete pixels on the surface of phantom. For example, if the surface assumed to be captured by CCD is a representation of 5×15 virtual detectors (Fig. 2), each one of which is calculated for the photon density, then $m = 75$. The maximum average error at each projection position can be defined as well:

$$e_{i,\max} = \max_j(|d_{ij} - s_{ij}|/s_{ij}). \qquad (11)$$

Figure 3 shows the comparisons between dynamic mode and step-mode, and Table 2 shows the average error and maximum average error of each projection at both angular velocities.

As a supplement to the simulation of the intensity profiles, comparisons of tomography reconstruction between step-mode and dynamic mode were also made. Figure 4 shows the reconstruction results with single target. The target was a sphere with a 0.5-mm diameter embedded in the phantom. The slice on $z = 1.5$ cm, which was the z-axis position of the center of the target, was selected to observe the reconstruction results. The 3D plots of the results are shown as well.

3.2. *Comparison between dynamic mode and step-mode with dual targets*

Similar to Sec. 3.1, comparisons between dynamic mode and step-mode with dual targets were made. In the simulation, two fluorescence targets with the same absorption coefficient were embedded in the lung of the phantom with an edge-to-edge distance of 3 mm. Each target was a sphere of 0.5 mm in diameter.

Figure 5 shows the comparison of photon intensities between two modes and Fig. 6 shows the reconstruction results with the forward data obtained with two modes. Table 3 shows the average error and maximum average error at each projection position with both angular velocities.

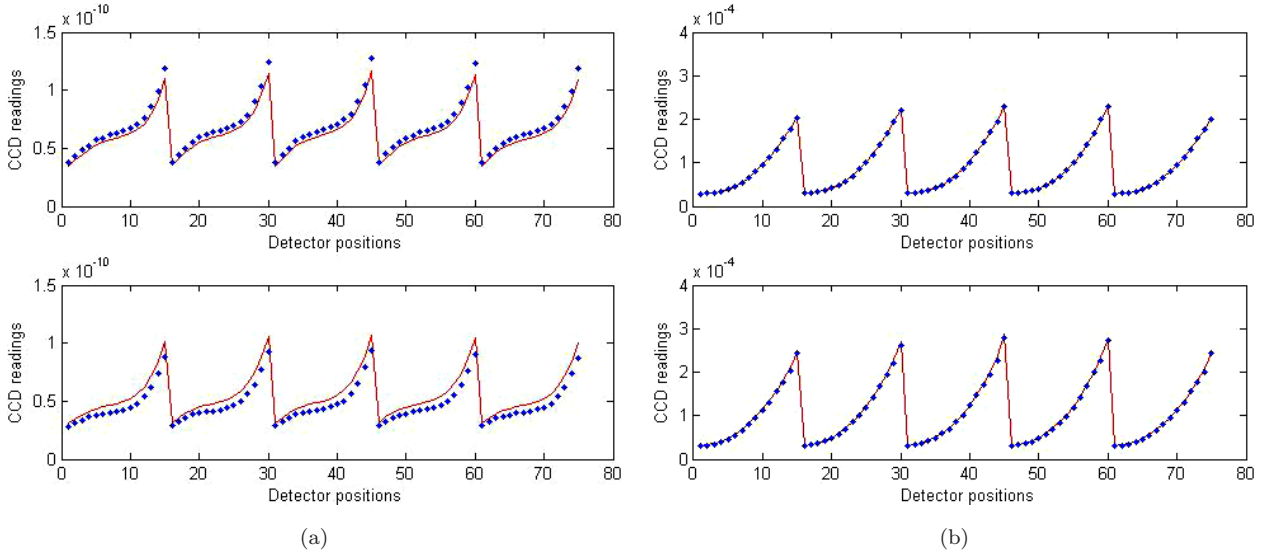

(a) (b)

Fig. 3. Comparisons between dynamic mode and step-mode with different angular velocity. (a)–(h) represent eight different projections' images of CCD. The dots represent the readings of CCD in step-mode and the lines represent the readings of CCD in dynamic mode. In each part of the figure, the upper plots are obtained at the angular velocity of 1°/s while the others are at the angular velocity of 2°/s.

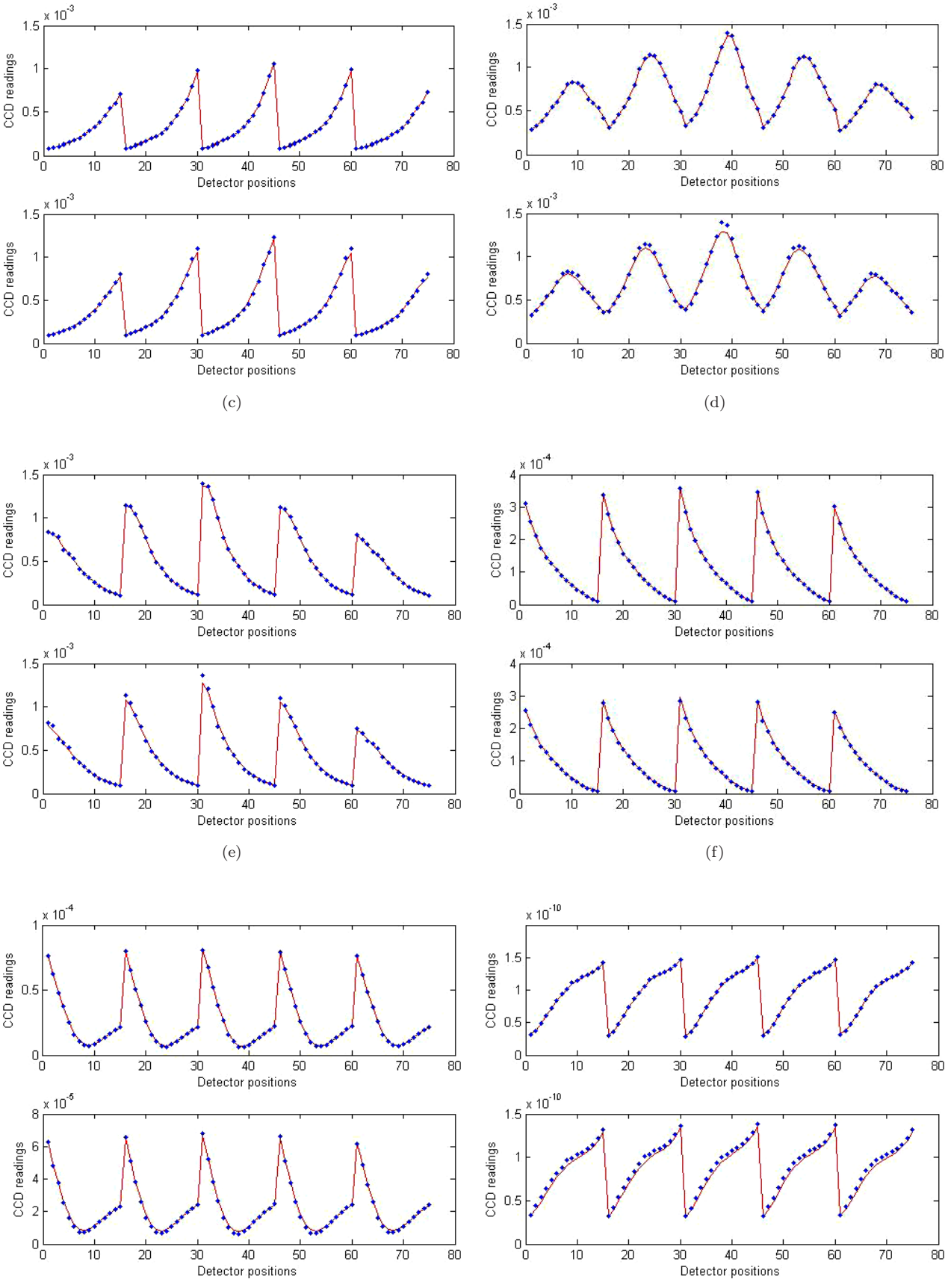

Fig. 3. (*Continued*)

Table 2. The average error and maximum average error at each projection position.

	1°/s		2°/s	
Projection	Average error (%)	Maximum average error (%)	Average error (%)	Maximum average error (%)
Start from 0° position	6.7	8.6	14.2	18.1
Start from 48° position	0.7	1.8	2.7	5.2
Start from 96° position	0.8	2.9	2.6	6.3
Start from 144° position	1.2	4.6	3.1	7.4
Start from 192° position	1.1	4.6	2.5	6.5
Start from 240° position	1.3	7.9	5.5	31.7
Start from 288° position	2.1	9.9	6.8	31.6
Start from 336° position	0.9	5.9	4.7	9.2

4. Discussion

The dynamic sampling mode for FMT is proposed and the feasibility of this imaging mode is investigated through simulations. Studies on both intensity profiles and tomography reconstructions are made in the simulations. From the plots (Fig. 3 and Fig. 5), it can be found that both the shape and the trend of the curves at different projection positions in dynamic mode are similar to those in step-mode. Some plots of the projections demonstrate the obvious differences between two imaging modes (Figs. 3(a), (d), (e) and Figs. 5(a), (c), (d) and (e)). Those figures also show that when the angular velocity is set to 2°/s , the intensity curves do not agree well with the curves of step-mode as those when the angular velocity is set to 1°/s, which indicates that increasing the angular velocity will increase the error of the intensity profiles in dynamic mode. The average errors and the maximum average errors of the two angular velocities at each projection position in dynamic mode (Table 2 and Table 3) show that both the average error and the maximum average error grow larger when the angular velocity increases from 1°/s to 2°/s.

How would the intensity error of dynamic mode impact the reconstruction performance? The reconstruction with dynamic sampling data can be viewed as a supplement to the simulation experiments, making the correlation between the estimated error in the simulated photon density and the accuracy in the expected reconstructions more visual and evident. Results illustrate that the measurement errors in dynamic mode with the angular velocity of 2°/s do compromise the reconstruction performance (Fig. 4(d) and Fig. 6(d)). In the single-target simulation, the reconstructed target in dynamic mode at the speed of 1°/s (Fig. 4(b)) is nearly the same as the one in step-mode (Fig. 4(a)), and the error between the reconstructed target's position and the real position is less than 0.05 mm. On the other hand, the target in dynamic mode at the speed of 2°/s , though is reconstructed in a correct position, produces false positives in the background (Fig. 4(d)), which compromise the positioning of the target. In the dual-target simulation, the angular velocity of 1°/s seems to have little influence on the reconstruction performance (Fig. 6(b)) compared with the reconstruction in step-mode, while 2°/s gives rise to the inaccurate reconstructed intensity since the intensities of the two targets were set the same in simulation.

According to Tikhonov regularization,[25] the regularization parameter α can be chosen to solve Eq. (8) and make the approximation solution, $\widetilde{x}$, to satisfy

$$\|\widetilde{x} - x\| \leq \sqrt{\alpha}\|v_0\| + \|W^+\|\delta, \tag{12}$$

where x is the normal solution of $Wx = b$, and the vector v_0 satisfies $W'v_0 = -x$. W^+ is the generalized inverse of matrix W. The inequality (8) suggests the fluctuation range of the solution $\widetilde{x}$, given the fluctuation range of vector $\tilde{b}$. Such inequality can be used to explain how the error of intensity profile in dynamic mode influences the reconstruction performance when the norm is defined as infinite norm. Although the maximum average error is as large as nearly 30% at some projection positions in dynamic mode at the speed of 2°/s, it is not the main cause of the reconstruction error since the CCD readings at the corresponding projection positions have the order of magnitude lower than the projections closer to the target. For example, the intensity in dynamic mode at the speed of 2°/s that has the error of 33.8% (Fig. 5(f)) is up to

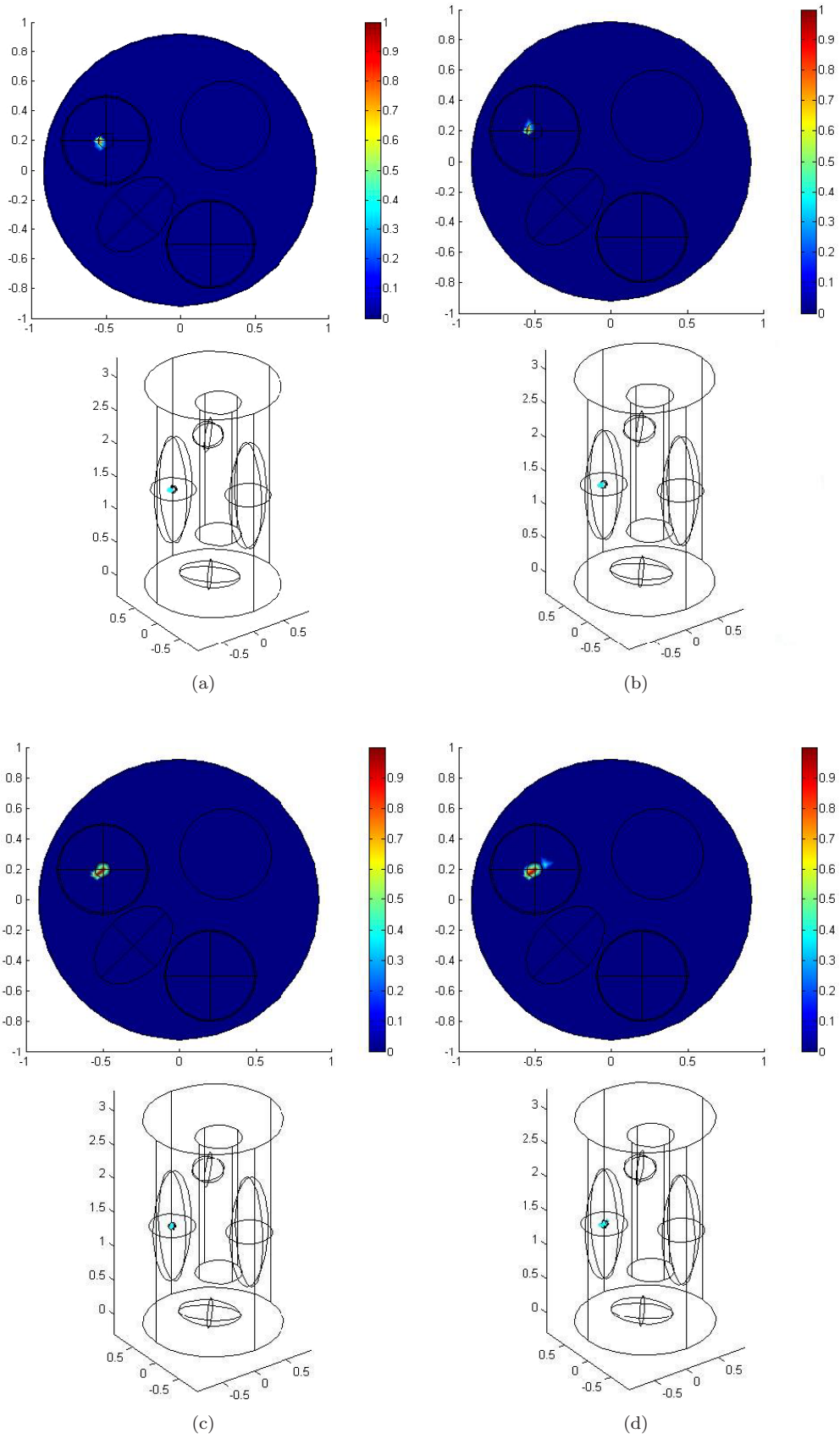

Fig. 4. Comparison of the phantom reconstruction results using the data from (a) and (c): step-mode, as well as (b) and (d): dynamic sampling mode. (b) and (d) represent the reconstruction results with 1°/s and 2°/s respectively. The black circle in each 2D slice shows the real position of the fluorescence target.

the magnitude of 10^{-3}, whereas the intensities in dynamic mode in Figs. 5(c) and 5(d) are up to the magnitude of 10^{-2}, which makes the large average error at the 6th projection position contribute little to inequality (12). This might be the reason that the reconstruction is not greatly impacted by the large maximum average error. Yet the reconstruction performance at the speed of 2°/s is not as good as it is at the speed of 1°/s due to the larger value of δ. When the intensity profiles in dynamic mode are in the range of allowable error (i.e., δ is not the large value), it would not cause large errors of the solution.

The reason why intensity curves of the dynamic mode do not agree very well with the curves of step-mode is the impact of motion artifact. During each exposure in the real experiment, as the phantom rotates, the emission photons reach the CCD plane in every angle rather than the fixed projection angle in the step-mode. The CCD readings after each exposure are viewed as the information of actual emission of fluorescent targets, thus constructing the artifact. Furthermore, the simulations depict the generation of motion artifact well. However, from the reconstruction results and the analysis above, it can be seen that the error in the forward

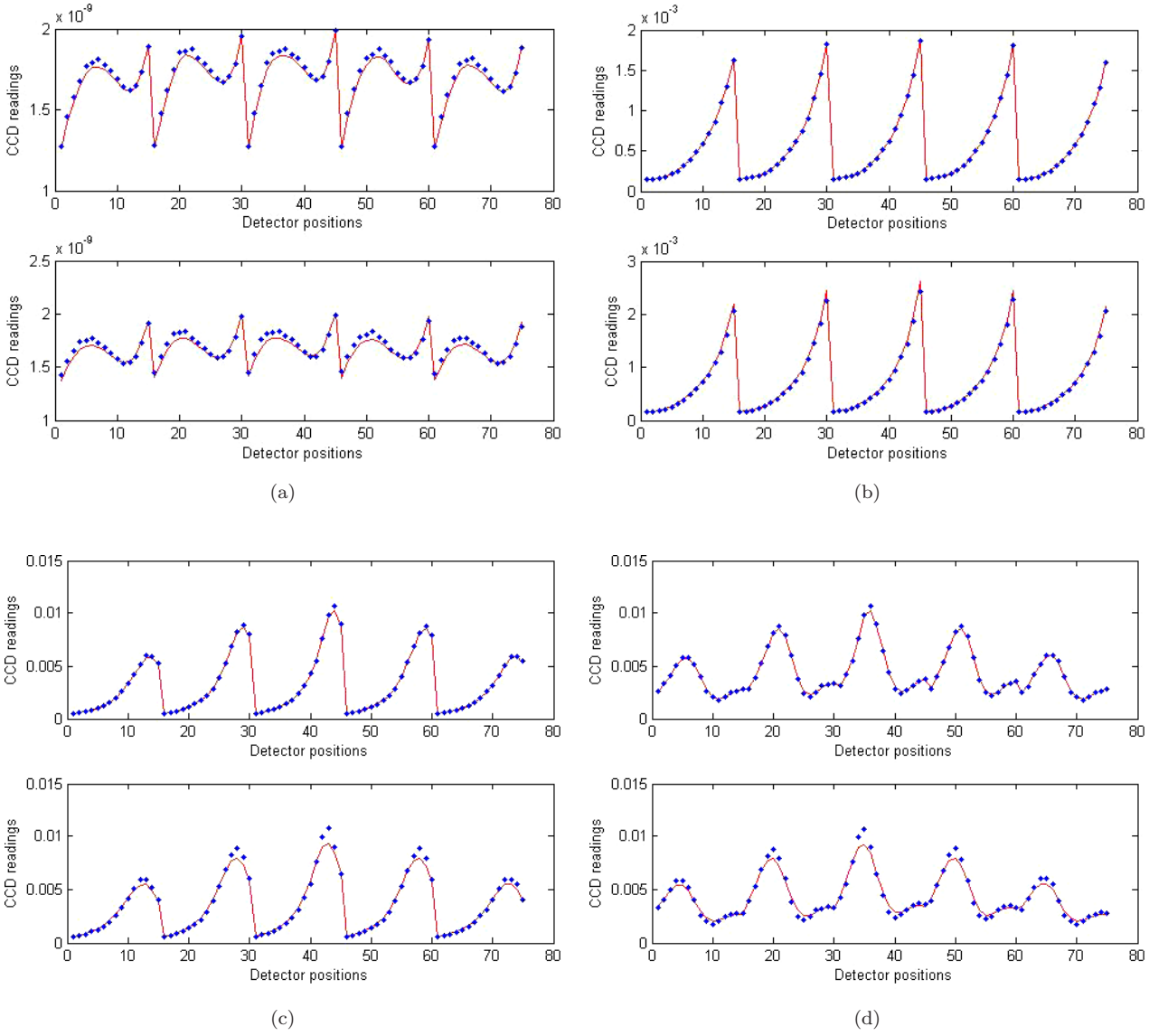

Fig. 5. Comparisons between dynamic mode and step-mode with different angular velocity in the simulation with dual targets. (a)–(h) represent eight different projections' images of CCD. The dots represent the readings of CCD in step-mode and the lines represent the readings of CCD in dynamic mode. In each part of the figure, the upper plots are obtained at the angular velocity of 1°/s while the others are at the angular velocity of 2°/s.

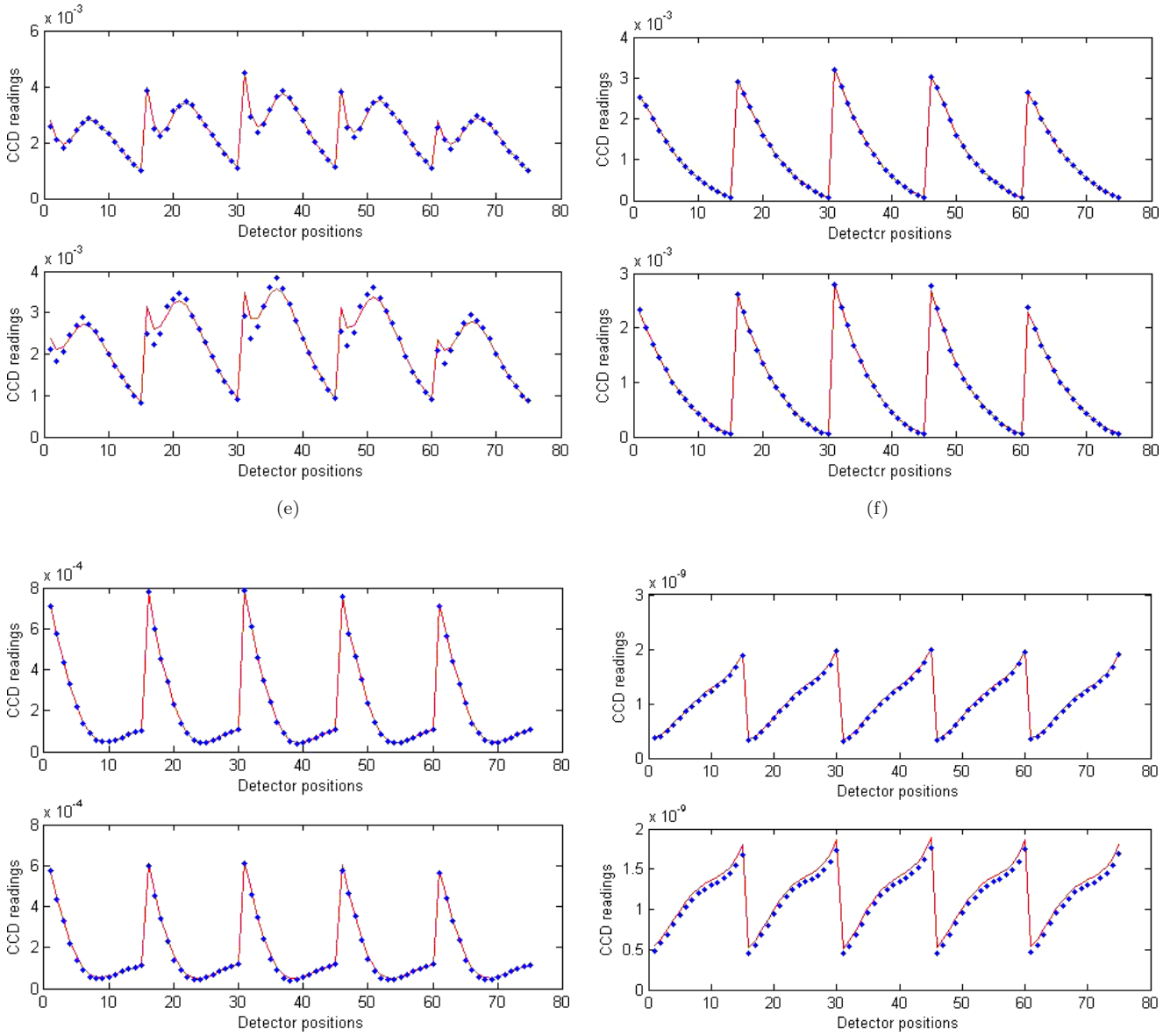

Fig. 5. (*Continued*)

Table 3. The average error and maximum average error at each projection position.

	1°/s		2°/s	
Projection	Average error (%)	Maximum average error (%)	Average error (%)	Maximum average error (%)
Start from 0° position	1.4	2.9	2.2	4.5
Start from 48° position	0.9	3.0	4.3	8.7
Start from 96° position	1.3	3.7	5.2	13.7
Start from 144° position	2.2	9.0	7.1	26.4
Start from 192° position	1.8	8.9	4.8	26.1
Start from 240° position	1.3	8.4	5.1	33.8
Start from 288° position	2.1	10.7	7.1	33.1
Start from 336° position	4.1	7.4	7.0	14.4

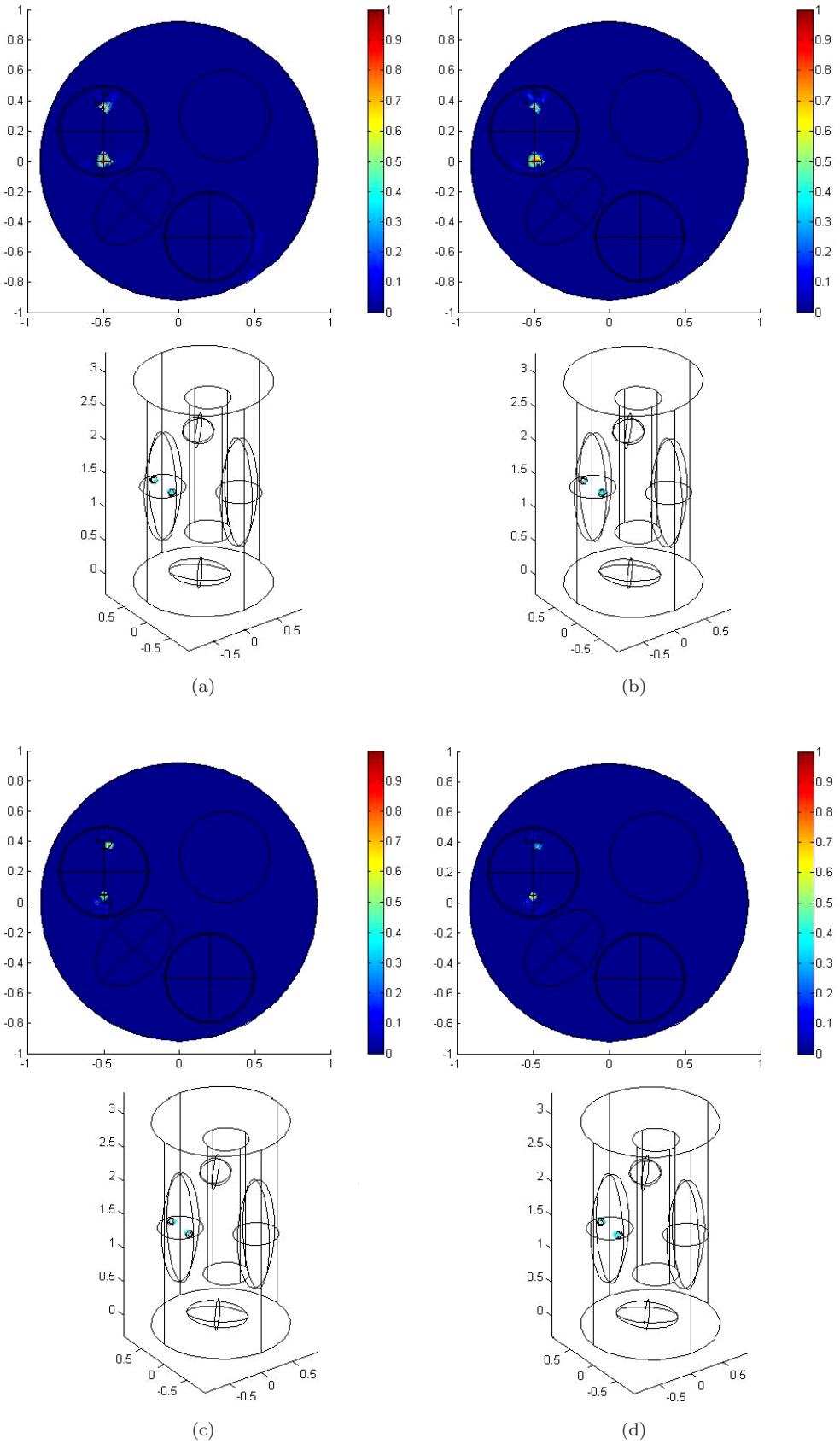

(a) (b) (c) (d)

Fig. 6. Comparison of the phantom reconstruction results with two targets using the data from (a) and (c): step-mode, as well as (b) and (d): dynamic sampling mode. (b) and (d) represent the reconstruction results with 1°/s and 2°/s respectively. The black circles in each 2D slice shows the real positions of two fluorescence targets.

data caused by the motion artifact does not give rise to the large error in the reconstruction results with the Tikhonov regularization.

In conclusion, we have demonstrated through the simulations that non-contact 360° FMT in a dynamic sampling mode has potential to provide reasonable imaging performance. The simulation results indicate that the heterogeneity within the turbid media does not compromise the reconstruction in the dynamic mode when the angular velocity is set in the appropriate value. Further work will focus on the application of dynamic sampling mode into small animals, in which the influence of irregular surface geometry on reconstruction would be studied specifically. Some other factors that might influence the accuracy of the intensity profiles and the reconstruction, for example, the exposure time of CCD and the position of the target, will be investigated, and some algorithms should be developed to reduce the motion effect and improve the reconstructions. Since the main challenge that dynamic mode meets is a loss of data caused by the readout time on CCD, we should take account of it in real experiments and seek the solution. Real experiments on the comparison between step-mode and dynamic mode will also be carried out to demonstrate that our suggested mode has the potential to overcome the obstacles caused by step-mode, and the optimal angular velocity in dynamic mode is going to be determined.

Acknowledgments

This work was partially supported by the National Natural Science Foundation of China, the Tsinghua-Yue-Yuen Medical Science Foundation, the National Basic Research Program of China, the High-Tech Research and Development Program of China, and the Special Research Fund for the Doctoral Program of Higher Education of China.

References

1. Ntziachristos, V., "Fluorescence molecular imaging," *Annu. Rev. Biomed. Eng.* **8**, 1–33 (2006).
2. Deliolanis, N., Lasser, T., Hyde, D., Soubret, A., Ripoll, J. and Ntziachristos, V., "Free-space fluorescence molecular tomography utilizing 360° geometry projections," *Opt. Lett.* **32**(4), 382–384 (2007).
3. Graves, E. E., Weissleder, R. and Ntziachristos, V., "Fluorescence molecular imaging of small animal tumor models," *Curr. Mol. Med.* **4**, 419–430 (2004).
4. O'Leary, M. A., Boas, D. A., Li, X. D., Chance, B. and Yodh, A. G., "Fluorescence lifetime imaging in turbid media," *Opt. Lett.* **21**, 158–160 (1996).
5. Chang, J., Graber, H. L. and Barbour, R. L., "Luminescence optical tomography of dense scattering media," *J. Opt. Soc. Am. A* **14**, 288–299 (1997).
6. Graves, E. E., Ripoll, J., Weissleder, R. and Ntziachristos, V., "A submillimeter resolution fluorescence molecular imaging system for small animal imaging," *Med. Phys.* **30**, 901–911 (2003).
7. Meyer, H., Garofalakis, A., Zacharakis, G., Psycharakis, S., Mamalaki, C., Kioussis, D., Economou, E. N., Ntziachristos, V. and Ripoll, J., "Noncontact optical imaging in mice with full angular coverage and automatic surface extraction," *Appl. Opt.* **46**, 3617–3627 (2007).
8. Ripoll, J., Schulz, R. B. and Ntziachristos, V., "Free-Space Propagation of Diffuse Light: Theory and Experiments," *Phys. Rev. Lett.* **91**, 103901 (2003).
9. Schulz, R. B., Ripoll, J. and Ntziachristos, V., "Experimental fluorescence tomography of tissues with noncontact measurements," *IEEE Transact. on Med. Imag.* **23**(4), 492–500 (2004).
10. Schulz, R. B., Echner, G., Ruhle, H., Stroh, W., Vierling, J., Vogt, T., Peter, J. and Semmler, W., "Development of a fully rotational noncontact fluorescence tomographer for small animals," *IEEE Nuclear Science Symposium Conference Record*, 0-7803-9221-3 (2005).
11. Arridge, S. R., Schweiger, M., Hiraoka, M. and Delpy, D. T., "A finite element approach for modeling photon transport in tissue," *Med. Phys.* **20**, 99–309 (1993).
12. Cong, A. and Wang, G., "A finite-element-based reconstruction method for 3D fluorescence tomography," *Opt. Express* **13**, 9847–9857 (2005).
13. Shives, E., Xu, Y. and Jiang, H., "Fluorescence lifetime tomography of turbid media based on an oxygen-sensitive dye," *Opt. Express* **10**, 1557–1562 (2002).
14. Milstein, A. B., Webb, K. J., Bouman, C. A., Zhang, Q., Boas, D. A. and Milane, R. P., "Fluorescence optical diffusion tomography," *Appl. Opt.* **42**, 3081–3094 (2003).
15. Jiang, H., "Frequency–domain fluorescent diffusion tomography: A finite-element-based algorithm and simulations," *Appl. Opt.* **37**, 5337–5343 (1998).
16. Roy, R., Godavarty, A. and Sevick-Muraca, E. M., "Fluorescence-enhanced optical tomography using referenced measurements of heterogeneous media," *IEEE Transactions on Medical Imaging*, 0278–0062 (2003).
17. Haskell, R. C., Svaasand, L. O., Tsay, T. T., Feng, T. C., McAdams, M. S. and Tromberg, B. J., "Boundary conditions for the diffusion equation in

radiative transfer," *J. Opt. Soc. Am. A* **11**, 2727–2741 (1994).
18. Schweiger, M., Arridge, S. R., Hirauka, M. and Delpy, D. T., "The finite element method for the propagation of light in scattering media: Boundary and source conditions," *Med. Phys.* **22**, 1779–1792 (1995).
19. Song, X., Wang, D., Chen, N., Bai, J. and Wang, H., "Reconstruction for free-space fluorescence tomography using a novel hybrid adaptive finite element algorithm," *Opt. Express* **15**, 18300–18317 (2007).
20. Tikhonov A. N. and Arsenin, V. Y., *Solution of Ill-Posed Problems* (Winston, Washington, D.C.: 1977).
21. Yao, J., Hu, G. and Bai, J., "Light propagation in free-space for non-contact near-infrared fluorescence tomography: Modeling and validation," *Journal of Infrared and Millimeter Waves*, ID 27378, in peer review.
22. Ripoll, J., Schulz, R. B. and Ntziachristos, V., "Free-space propagation of diffuse light: Theory and experiments," *Phys. Rev. Lett.* **91**(10), 103901 (2003).
23. Lv, Y., Tian, J., Cong, W., Wang, G., Luo, J., Yang, W. and Li, H., "A multilevel adaptive finite element algorithm for bioluminescence tomography," *Opt. Express* **14**, 8211–8223 (2006).
24. Alexandrakis, G., Rannou, F. R. and Chatziioannou, A. F., "Tomographic bioluminescence imaging by use of a combined optical-PET (OPET) system: A computer simulation feasibility study," *Phys. Med. Biol.* **50**, 4225–4241 (2005).
25. Kuhnert, *Generalized Inverse Matrix and Regularization Method* (High Education Press, Beijing, 1985) [in Chinese].